Research Paper

Multimodal imaging of the receptor for advanced glycation end-products with molecularly targeted nanoparticles

Christian J. Konopka[1,2] *, Marcin Wozniak[3,4] *, Jamila Hedhli[1,2], Agata Ploska[2,3,4], Aaron Schwartz-Duval[1], Anna Siekierzycka[3], Dipanjan Pan[1,2], Gnanasekar Munirathinam[5], Iwona T. Dobrucki[2], Leszek Kalinowski[3,4] ✉, Lawrence W. Dobrucki[1,2,3,4] ✉

1. Department of Bioengineering, University of Illinois at Urbana-Champaign, Urbana, IL
2. Beckman Institute for Advanced Science and Technology, Urbana, IL
3. Department of Medical Laboratory Diagnostics and Central Bank of Frozen Tissues & Genetic Specimens, Medical University of Gdansk, Gdansk, Poland
4. Biobanking and Biomolecular Resources Research Infrastructure Poland (BBMRI.PL), Gdansk, Poland
5. Department of Biomedical Sciences, University of Illinois College of Medicine, Rockford, IL

* These authors contributed equally to these studies

✉ Corresponding authors: Lawrence W. Dobrucki, Ph.D. University of Illinois at Urbana-Champaign. 405 N Mathews Ave, MC-251, Urbana, IL 61801. e-mail: dobrucki@illinois.edu; phone: +1 217-244-3938; Leszek Kalinowski, M.D. Ph.D. Medical University of Gdansk, Poland. Debinki Street 7, 80-211 Gdansk, Poland. e-mail: lekal@gumed.edu.pl; phone: +48 58 349-2791

Abstract

The receptor for advanced glycation end-products (RAGE) is central to multiple disease states, including diabetes-related conditions such as peripheral arterial disease (PAD). Despite RAGE's importance in these pathologies, there remains a need for a molecular imaging agent that can accurately assess RAGE levels *in vivo*. Therefore, we have developed a multimodal nanoparticle-based imaging agent targeted at RAGE with the well-characterized RAGE ligand, carboxymethyllysine (CML)-modified human serum albumin (HSA).

Methods: A multimodal tracer (^{64}Cu-Rho-G4-CML) was developed using a generation-4 (G4) polyamidoamine (PAMAM) dendrimer, conjugated with both rhodamine and copper-64 (^{64}Cu) chelator (NOTA) for optical and PET imaging, respectively. First, ^{64}Cu-Rho-G4-CML and its non-targeted analogue (^{64}Cu-Rho-G4-HSA) were evaluated chemically using techniques such as dynamic light scattering (DLS), electron microscopy and nuclear magnetic resonance (NMR). The tracers' binding capabilities were examined at the cellular level and optimized using live and fixed HUVEC cells grown in 5.5-30 mM glucose, followed by *in vivo* PET-CT imaging, where the probes' kinetics, biodistribution, and RAGE targeting properties were examined in a murine model of hindlimb ischemia. Finally, histological assessment of RAGE levels in both ischemic and non-ischemic tissues was performed.

Conclusions: Our RAGE-targeted probe demonstrated an average size of 450 nm, a Kd of 340-390 nM, rapid blood clearance, and a 3.4 times greater PET uptake in ischemic RAGE-expressing hindlimbs than their non-ischemic counterpart. We successfully demonstrated increased RAGE expression in a murine model of hindlimb ischemia and the feasibility for non-invasive examination of cellular, tissue, and whole-body RAGE levels with a molecularly targeted tracer.

Key words: receptor for advanced glycation end-products, PET-CT, hindlimb ischemia, multimodal imaging, inflammation

Introduction

The receptor for advanced glycation end-products (RAGE), a multi-ligand transmembrane receptor, has been identified as a key player in many disease states. The overexpression and activation by RAGE's ligands induce oxidative stress and inflammation known to contribute to the pathogenesis of several diabetes-related complications, neurodegenerative disorders, as well as numerous

cancer types [1, 2]. Yet despite RAGE's key features that make it ideal for targeted therapies and imaging in these conditions, a significant need remains for a nanoparticle-based imaging agent directed at RAGE[3].

The role of RAGE in diabetic complications is perhaps one of the most comprehensively studied. RAGE has been shown to contribute to diabetic neuropathy, nephropathy, cardiomyopathy, and ocular, arterial, and atherosclerotic diseases[4–8]. Often, RAGE's negative effects are present in diabetes-associated peripheral arterial disease (PAD), where it impairs the recruitment of collateral vessels and leads to ischemia. Studies utilizing diabetic murine models of hindlimb ischemia confirmed this involvement, by demonstrating that RAGE knockout animals show significantly enhanced perfusion and collateral vessel recruitment compared to their wildtype counterparts [9]. Additionally, although it has been observed that RAGE levels are increased even in non-diabetic PAD patients, this has not been extensively tested in preclinical models.

Currently, investigative therapeutic strategies aim to reduce the damaging effect of RAGE through attenuating RAGE signaling. This may be done either by decreasing the number of RAGE ligands, such as advanced glycation end products (AGEs), or by blocking the binding of RAGE with its ligands [10, 11]. One method of reducing AGE-RAGE interactions in diabetic patients is the administration of a conventional anti-diabetic treatment, thiazolidinediones (TZDs). TZDs exhibit an antidiabetic effect by inducing the activation of peroxisome proliferator-activated receptor (PPAR gamma), as well as reducing the number of membrane-bound RAGE molecules while simultaneously increasing secretory RAGE (esRAGE) receptors [12, 13]. esRAGE is a RAGE isomer that lacks a transmembrane domain, which allows it to act as a decoy receptor, further decreasing RAGE signaling. esRAGE has also been explored as a biomarker for various diabetic complications [14]. Similarly, soluble RAGE (sRAGE), which contains only the extracellular domain of RAGE, has been used as a therapeutic agent with medicinal value in atherosclerosis, wound healing, nephropathy, retinopathy, and neuropathy [3, 15–19]. Another promising therapeutic method is the use of AGE-binding DNA aptamers. These aptamers prevent the binding of AGEs and, consequently, block RAGE signaling, halting the progression of diabetic neuropathy [20].

Despite RAGE's importance and the future promise of RAGE-targeted treatments, there are few RAGE-targeted imaging tracers available to track RAGE levels during disease progression. A well-designed RAGE-targeted tracer could both improve diagnosis, as well as monitor anti-RAGE and conventional treatment responses. One previously developed tracer used [99mTc]-labeled polyclonal anti-RAGE antibodies for scintigraphy imaging of the proximal aorta in 20-week-old ApoE-/- mice. The same group extended this work and developed a [99mTc]-labeled monoclonal anti-RAGE antibody demonstrating improved specificity compared to the polyclonal antibody [21, 22]. This monoclonal antibody-based imaging agent demonstrated that RAGE-targeted molecular imaging can detect the effect of diabetes on RAGE expression in a diabetic murine model of hindlimb ischemia [23]. A recent paper demonstrated, using the previously synthesized radiolabeled antibody, enhanced RAGE expression in coronary and carotid fibroatheromas as well as in models for atherosclerosis in small arteries of large animal hind limbs [24]. Although studies in atherosclerosis and peripheral arterial disease confirm that RAGE overexpression can be successfully used as a target for molecular imaging, it has not been extensively evaluated in a non-diabetic milieu. Other RAGE-targeted tracers include a PET tracer that was developed using a recombinant [18F]-labeled S100A4 protein for PET imaging; however, it suffers from a lack of stability and affinity for RAGE [25].

Another probe, ([18F]) RAGR, is a RAGE-targeted small molecule, which crosses the blood brain barrier. This tracer confirmed the upregulation of RAGE in Alzheimer's disease and provided novel applications of RAGE-targeted PET imaging [26]. Despite the above-mentioned tracers' clear applications, there are limitations to both antibody imaging agents as well as small molecule imaging tracers. Antibody-based imaging agents suffer from a characteristically long blood-residence time, resulting in high background and lower quality images. Moreover, both antibody and small molecule imaging agents suffer from an inherent necessity to be single modality tracers with no drug payload capability and poor optimization for the number of binding ligands and reporter molecules [27, 28].

To address these limitations, researchers sought nanotechnology, which allows for unparalleled development of personalized treatments and assessment strategies. By engineering nanoparticles (NP) with highly specific targeting ligands, functionalizing the NPs for detection in multiple different imaging modalities, and charging them with effective drugs, cleverly designed nanoparticles can provide earlier detection, improved diagnoses, and controlled drug delivery methods [29–31]. One such platform researchers used to build targeted nanoparticles is poly(amidoamine) (PAMAM)

dendrimers. PAMAM dendrimers' unique surface allows them to be altered with peripheral functional groups and labels such as radionuclides, fluorophores, targeting ligands, drugs and more, rendering them useful in various diagnostic and therapeutic biomedical applications [32].

This study demonstrates the chemical synthesis, *in vitro* characterization, and *in vivo* imaging capabilities of a RAGE-targeted, PAMAM-based, multimodal imaging agent. Here we report the use of our multimodal nanoparticle construct for *in vitro* studies in live cells, *in vivo* small animal PET-CT imaging, and postmortem histologic evaluation of RAGE expression in a non-diabetic murine model of hindlimb ischemia.

Results

Chemical synthesis

RAGE-targeted ^{64}Cu-Rho-G4-CML and control ^{64}Cu-Rho-G4-HSA tracers were synthesized in a stepwise manner (**Figure S1**), to achieve the final product illustrated in **Figure 1**. Using previously described methods, the chelating agent p-SCN-Bn-NOTA was conjugated to 25% of the dendrimer primary amines for later chelation with ^{64}Cu radioisotope [33]. The amine-reactive tetramethyl-rhodamine succinimidyl ester was then chosen as a fluorophore. The final construct was targeted to RAGE by conjugating the well-characterized RAGE ligand, carboxymethyl-lysine (CML)-modified human serum albumin (HSA) (**Figure S2**) via a succinimidyl-(N-methyl-polyethylene glycol) PEG$_4$ spacer to enhance water solubility and improve pharmaco-kinetic properties. The number of CML-HSAs conjugated to the dendrimer surface (8) and the percentage of CML modification (20%) to HSA was optimized for RAGE binding affinity, and was determined experimentally (**Figure S3**). From each of step of the synthesis, small amounts of products were collected and evaluated with SDS-PAGE gel electrophoresis (**Figure S4**). The final nanoparticle constructs were visualized using transmission electron microscopy (TEM) and scanning electron microscopy with electron dispersion spectroscopy (SEM-EDS). TEM images that were analyzed to provide size information, and dynamic light scattering (DLS) measurements indicated an ~400 nm diameter, while SEM-EDS measurements confirmed the chelation of Cu atoms. Additionally, zeta-potential (Z-potential) was analyzed and a strongly anionic mean Z-potential of -37.6 mV ± 1.9 mV was observed (**Figure 1**). This property may contribute to the probe's low observed cytotoxicity and favorable stability profile for imaging (**Figure S5**

and **Figure S6**) [34].

The effect of hyperglycemic environment on RAGE

In this study, HUVECs were cultured in various glucose concentrations (5.5-30 mM), according to previous methods, for 12 or 24 h to assess RAGE mRNA expression [35]. Following both 12 and 24 h exposures to a hyperglycemic environment, RAGE expression was upregulated. *In vitro* observation indicated that incubation with 14 mM glucose for 12 h induced the highest RAGE mRNA levels (3.1 ± 0.22-fold increase vs. control) (**Figure S7**). Therefore, a 14 mM glucose concentration and 12 h time point were used for subsequent experiments.

Characterization of binding to AGE receptor

Both fluorescence and gamma well counting methods were used to determine the RAGE cellular binding characteristics of ^{64}Cu-Rho-G4-HSA and ^{64}Cu-Rho-G4-CML nanoparticles. HUVECs were cultured with low or high glucose levels, then cells were incubated with either ^{64}Cu-Rho-G4-HSA or ^{64}Cu-Rho-G4-CML. HUVECs' binding proceeded rapidly, reaching a plateau at about 30 min (**Figure 2A-B**). HUVECs were also incubated with various concentrations of ^{64}Cu-Rho-G4-HSA and ^{64}Cu-Rho-G4-CML for 2 h at 37 °C in both hyperglycemic (14 mM glucose) and normoglycemic (5.5 mM glucose) environments. Increased RAGE mRNA caused significantly higher ^{64}Cu-Rho-G4-CML uptake (1.8−3-fold) in high glucose cultured cells than in the control probe. In the normoglycemic milieu, ^{64}Cu-Rho-G4-CML binding declined, and ^{64}Cu-Rho-G4-HSA exhibited non-specific binding (**Figure 2C-D**). Further immunofluorescence and flow cytometry confirmed the targeted and non-targeted nanoparticles' binding specificity to RAGE. The targeted probe demonstrated a K_D of 338 ± 54 nM and 388 ± 9 nM (using fluorescence and gamma well counting methods, respectively, see **Figure 2E-F**). Competitive inhibition studies using flow cytometry demonstrated reduced RAGE binding (up to 80%) at various concentrations of ^{64}Cu-Rho-G4-CML when cells were pretreated with anti-RAGE antibody. Furthermore, targeted nanoparticles showed significantly higher colocalization with RAGE as compared to the control probe when analyzed using confocal microscopy. Results from colocalization analysis include Manders' coefficients of 0.86 ± 0.08 and 0.98 ± 0.01 and Pearson's R of 0.77 ± 0.03 for targeted nanoparticles vs. Manders' coefficients of 0.59 ± 0.18 and 0.47 ± 0.07 and Pearson's R of 0.30 ± 0.15 for non-targeted nanoparticles (**Figure 3A-C**). Additionally, flow cytometry analysis demonstrated

significantly more staining of RAGE-expressing cells using the targeted vs. control probe (**Figure 3D-E**).

In vivo evaluation in preclinical model of PAD

Following *in vitro* validation and probe optimization, ^{64}Cu-Rho-G4-CML and ^{64}Cu-Rho-G4-HSA were studied *in vivo*. First, we determined the probe's optimal imaging time and biodistribution. Dynamic 60-min PET-CT imaging (**Figure 4A**) was performed to generate blood (BAC) and tissue (TAC) activity curves (**Figure 4B**). After the imaging session,

animals were euthanized and selected tissues were collected for gamma well counting (GWC) to quantify the biodistribution profiles of ^{64}Cu-Rho-G4-CML and ^{64}Cu-Rho-G4-HSA (**Figure 5**). Both ^{64}Cu-Rho-G4-CML and ^{64}Cu-Rho-G4-HSA demonstrated favorable pharmacokinetics and blood clearance, reaching ~5% of initial blood activity within 1 h. The tracers primarily followed a hepatobiliary excretion route, with significant uptake in the liver and intestines [36].
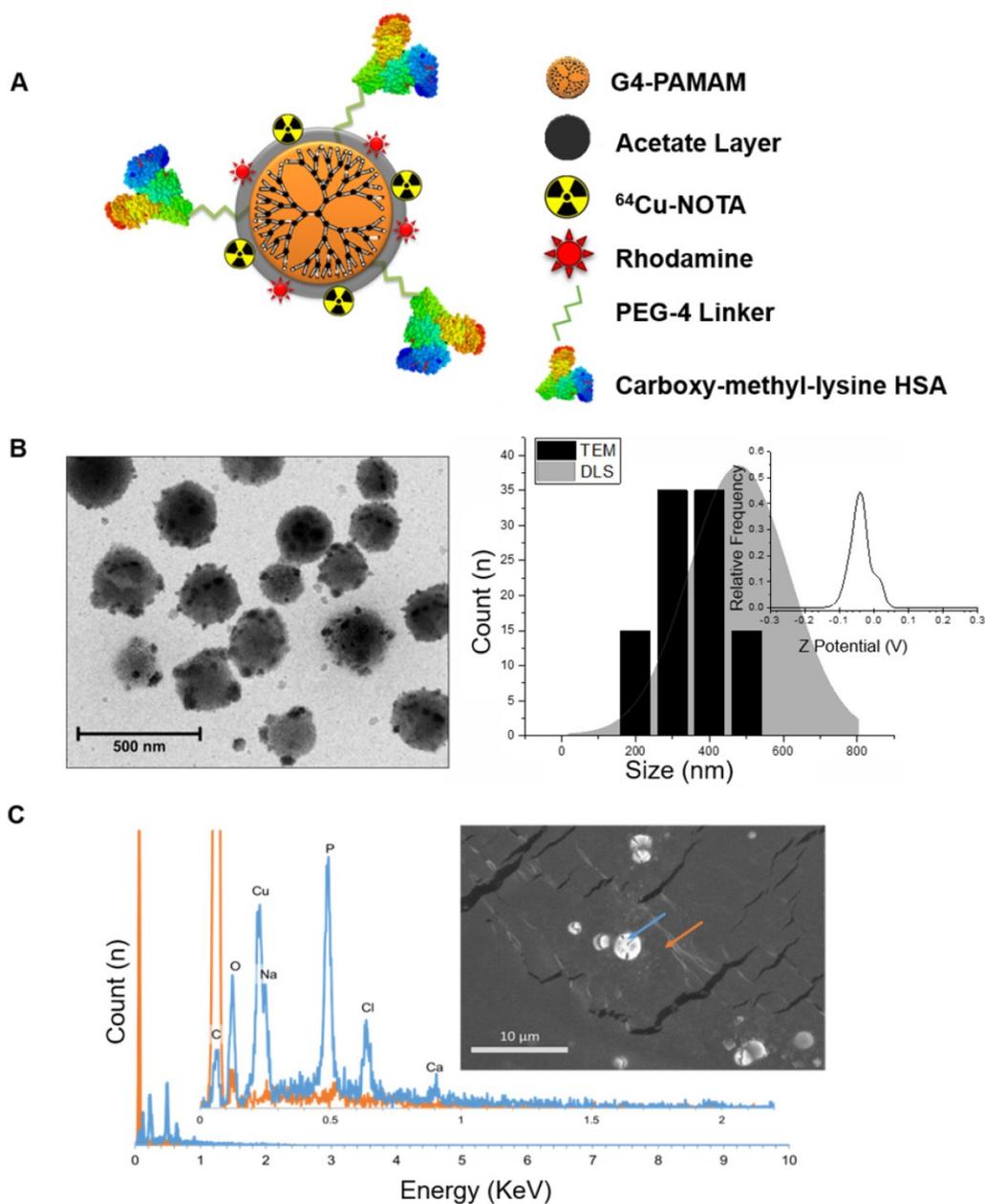
Figure 1. Physicochemical characterization of RAGE-targeted nanoparticles. **(A)** Schematic diagram of the multimodal (PET-optical) ^{64}Cu-Rho-G4-CML nanoparticle construct. **(B)** Zeta-potential and size distributions of ^{64}Cu-Rho-G4-CML are presented. Particle diameters were obtained through ImageJ analysis of TEM (representative images shown) and DLS measurements. **(C)** Electron-dispersion spectra of ^{64}Cu-Rho-G4-CML (blue) and background (orange) as obtained through EDS-scanning electron microscopy.
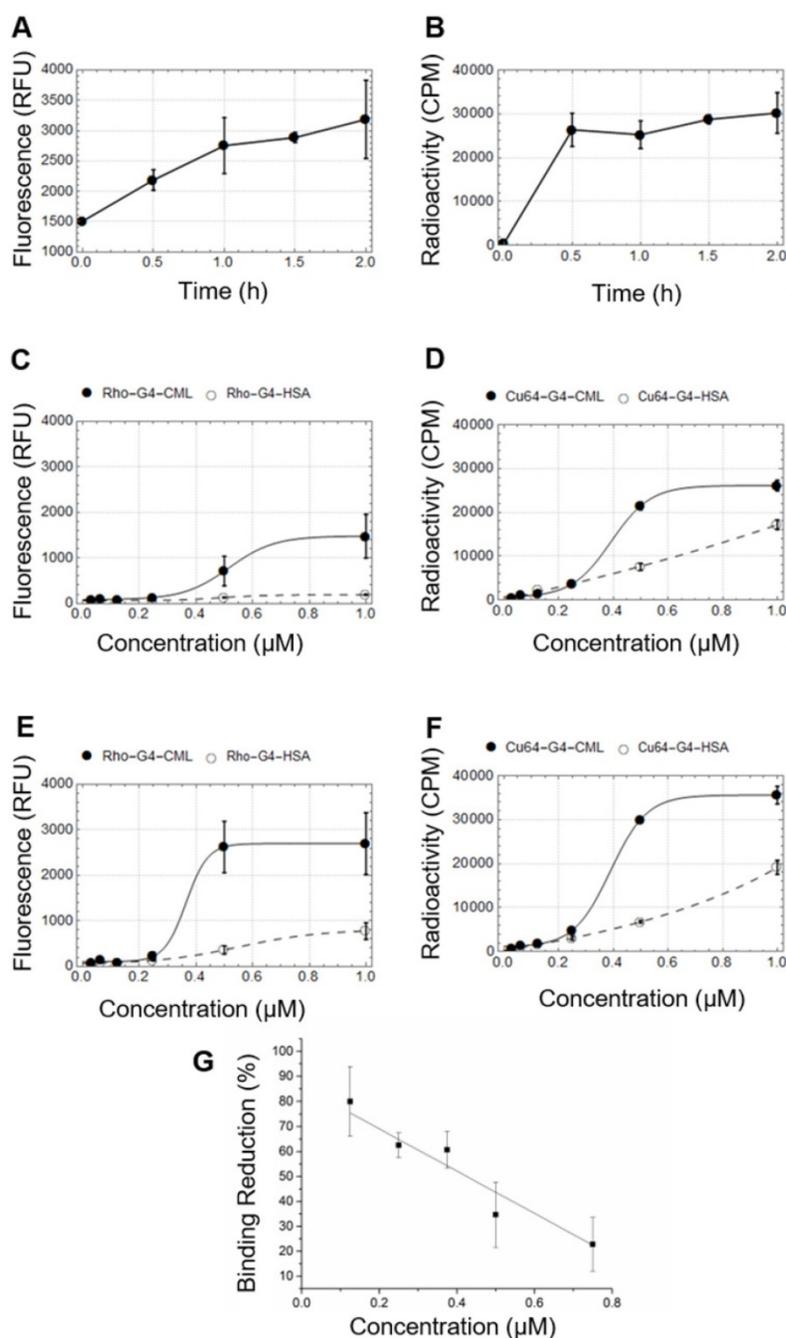
Figure 2. *In vitro* cellular binding studies in human umbilical vein endothelial cells (HUVEC). Temporal changes in cellular binding were studied using fluorescence **(A)** and gamma well counting **(B)**. HUVECs were grown in normoglycemic (5.5 mM glucose) **(C-D)** or hyperglycemic (14 mM glucose) **(E-F)** conditions before incubation with multimodal targeted (^{64}Cu-Rho-G4-CML, solid line) and non-targeted (^{64}Cu-Rho-G4-HSA, dashed line) nanoparticles. Both, fluorescence **(C, E)** and radioactivity, **(D, F)** were measured at various concentrations of the probes (0–1 μM). **(G)** HUVECs pretreated with RAGE antibody and incubated with various concentrations of G4-CML (0–0.75 μM) demonstrated significantly reduced binding compared to untreated cells incubated in the same G4-CML concentrations.

Mice were then subjected to serial PET-CT imaging 1 and 2 weeks after surgical ligation of the right femoral artery with either ^{64}Cu-Rho-G4-CML (n=6) or ^{64}Cu-Rho-G4-HSA (n=6) delivered by jugular vein injection (**Figure 6**). At one week post-surgery, mice imaged 2 h after intravenous injection of

^{64}Cu-Rho-G4-CML exhibited 3.4 times greater uptake in ischemic hindlimbs (expressed as % injected dose by tissue weight, %I.D./g) than the non-ischemic hindlimb. The uptake of non-targeted ^{64}Cu-Rho-G4-HSA remained low and comparable in both ischemic and non-ischemic hindlimbs. At two weeks post-surgery, the difference was no longer observed between ischemic and non-ischemic uptake (**Figure 7**).

Postmortem analysis

Immediately following the terminal imaging study (1 or 2 weeks after surgical ligation of the right femoral artery), mice were sacrificed and tissues were collected for both GWC and histological analysis. RAGE expression in ischemic hindlimbs at 1 and 2 weeks post-ligation was examined using quantitative immunofluorescent staining with anti-RAGE antibody (**Figure 8**). Ischemic hindlimbs at 1 week post ligation demonstrated significantly higher RAGE staining as compared to the non-ischemic muscle sections (16.70 ± 2.48 vs. 7.78 ± 1.07 % positive area, P < 0.05). At 2 weeks post ligation, RAGE-positive staining in ischemic hindlimb returned to the non-ischemic levels.

Discussion

This study illustrates the utility of non-invasive multimodal imaging with a molecularly targeted nanoparticle for detecting RAGE expression in a non-diabetic model of hindlimb ischemia. The timely significance of such an imaging agent is notable given the substantial prevalence of PAD and its correlation with morbidity or mortality of other atherosclerotic diseases [37]. The performed experiments elucidate enhanced RAGE expression in both hyperglycemic cultured endothelial cells as well as in normoglycemic animals subjected to hindlimb ischemia. The integration of both nuclear and fluorescent labels broadened the imaging agent's utility, allowing its use in cellular analyses, live animal PET imaging, and histological evaluations.
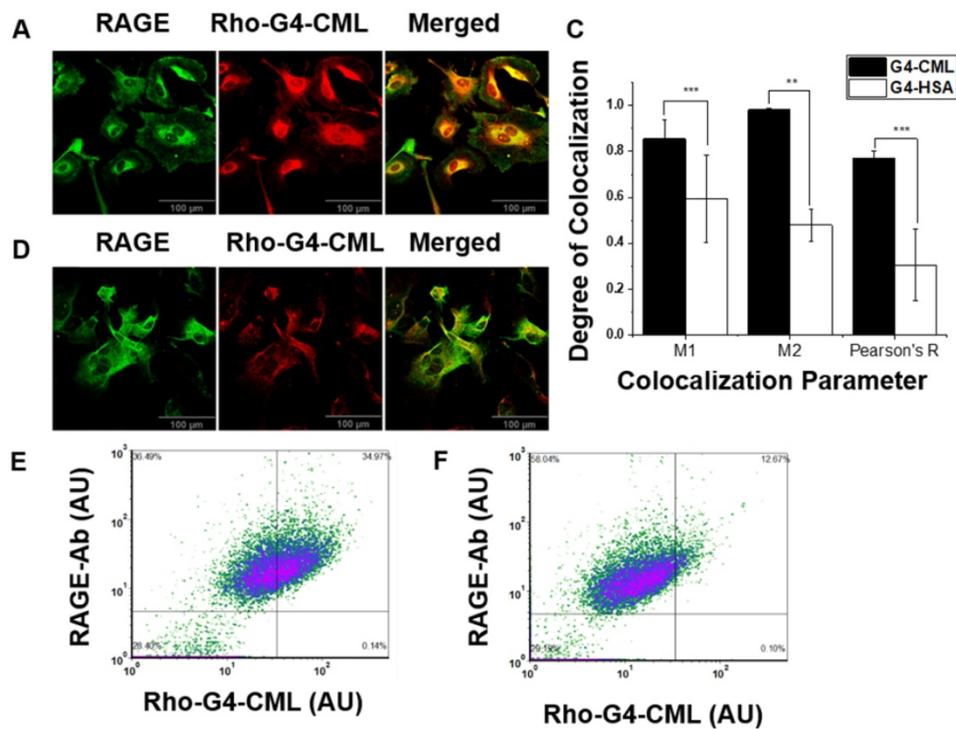
Figure 3. *In vitro* single cell colocalization studies. Confocal microscopy of HUVECs grown in hyperglycemic conditions (14 mM glucose) and incubated with 1 µM RAGE-targeted (Rho-G4-CML) **(A)** and non-targeted control nanoparticle (Rho-G4-has) **(B)**. **(C)** Colocalization of Rho-G4-CML and Rho-G4-HSA with RAGE antibody was analyzed using FIJI and Manders' coefficients and Pearson's R values are presented. Specificity of the cellular binding of RAGE-targeted nanoparticle was confirmed by flow cytometry in HUVECs incubated with Rho-G4-CML **(D)** or Rho-G4-HSA **(E)** and co-incubated with anti-RAGE antibody labeled with FITC.
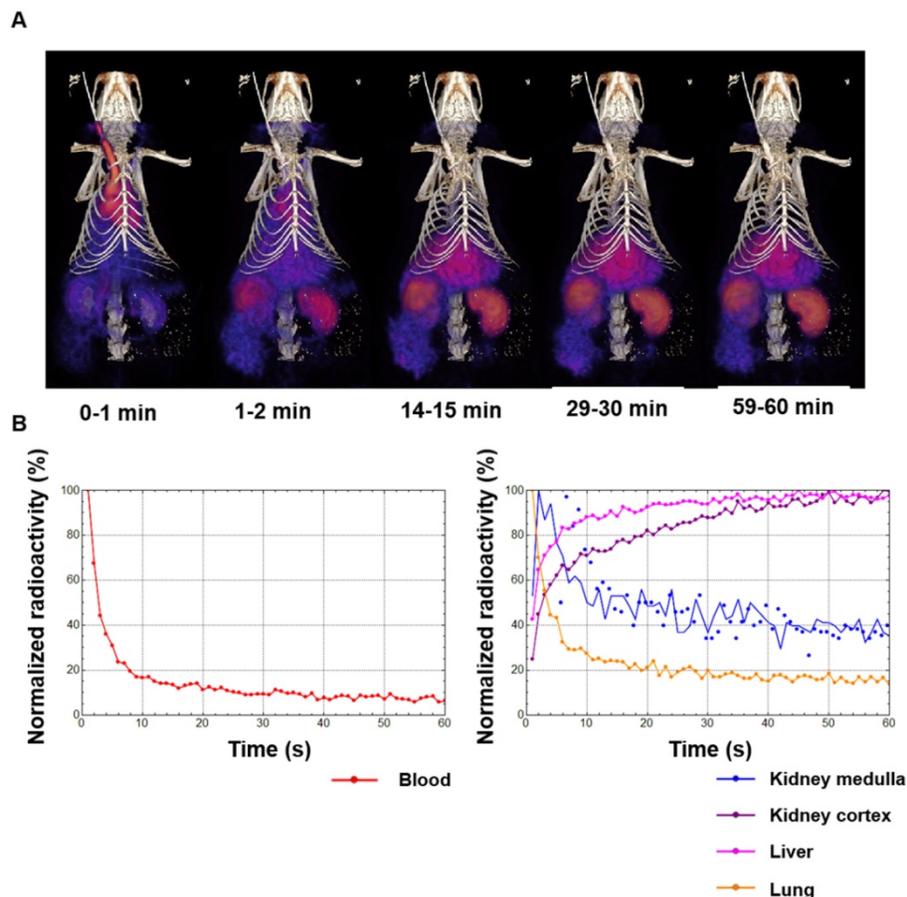
Figure 4. (A) Dynamic PET-CT images during the first 60 min after intravascular injection of ^{64}Cu-Rho-G4-CML nanoparticle targeted at RAGE. **(B)** Dynamic PET-CT images were analyzed to plot blood-activity-curve (BAC) and selected tissue-activity-curves (TAC). ^{64}Cu-Rho-G4-CML cleared quickly from the blood and demonstrated both renal and hepatobiliary excretion routes.
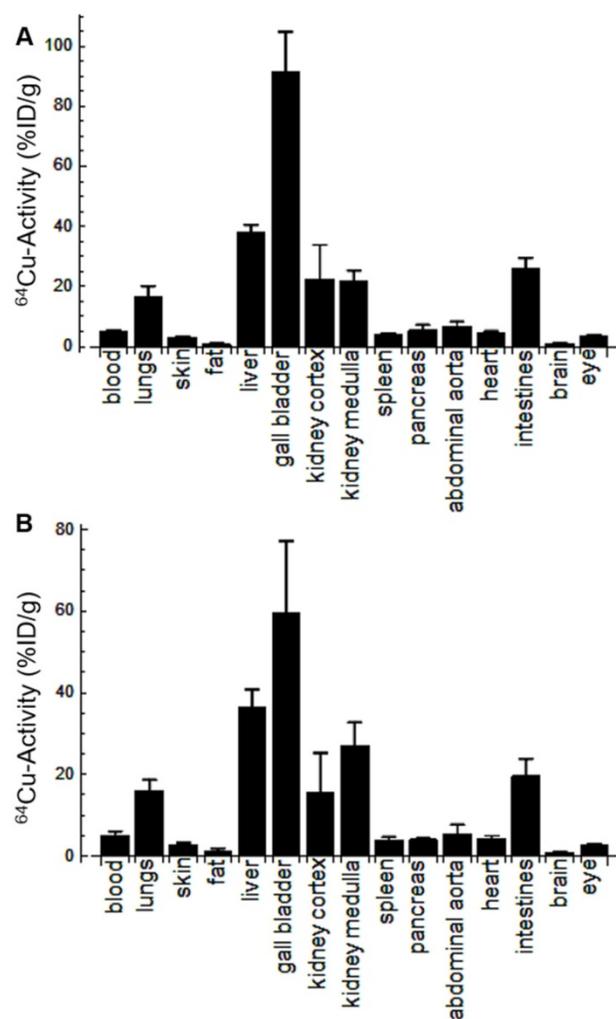
Figure 5. Biodistribution of ^{64}Cu-Rho-G4-CML **(A)** and ^{64}Cu-Rho-G4-HSA **(B)** in select organs at 90 min after intravascular injection via the jugular vein of C57BL/6 mice. Results are expressed in percentage of injected dose per gram tissue (%ID/g). These results demonstrate comparable biodistribution between targeted (^{64}Cu-Rho-G4-CML) and non-targeted (^{64}Cu-Rho-G4-HSA) nanoparticles and relatively low non-specific uptake in other critical organs.

Cellular analysis

Previous studies by other groups demonstrated that elevated endothelial glucose levels increased the expression of inflammatory genes, such as *RAGE*, *NF-κB p50*, *IL8* and *IL6* [33]. After confirming the induced overexpression of RAGE in HUVECs cells, these cells were used for a variety of characterizations, which demonstrated high affinity binding of the nanoparticle in RAGE-expressing HUVECs. Both fluorescence and radiometric assays were performed, allowing for direct correlation between fluorescence and nuclear signals. This validation confers on the probe a utility for quantitative examination of probe uptake, using both nuclear and optical signals at both whole body and cellular levels. Therefore, potential applications of this probe are not limited to diabetic conditions but many types of inflammatory conditions that involve the RAGE/AGE axis.

Live animal PET imaging

For our investigations, we used a well-characterized animal model of hindlimb ischemia, in which surgical ligation of the femoral artery in C57BL/6J mice accurately mimics PAD [38]. Previously published RAGE imaging studies using single photon emission computed tomography (SPECT) with radiolabeled mAb fragments detected increased RAGE expression in diabetic animals [23, 39]. However, this probe was limited by slow blood pool clearance and low specific uptake, which contributed to a relatively high background. In contrast, we evaluated ^{64}Cu-Rho-G4-CML as the first multimodal nanoparticle-based RAGE-targeted tracer for *in vivo* positron emission tomography (PET) imaging of RAGE in non-diabetic animals subjected to hindlimb ischemia, with about 1.6 times higher ischemic to non-ischemic leg uptake ratio than that reported by other groups.

C57BL/6J mice underwent surgical ligation of the right femoral artery to induce unilateral hindlimb ischemia. The findings of this study demonstrated a clear time course of inflammation in non-diabetic induced hindlimb ischemia, which was evidenced by high RAGE expression followed by a return of RAGE to basal levels after 2 weeks. This finding is in accordance with previous genome-based studies, which found that transcription of inflammation mediators following femoral artery ligation were the largest functional gene cluster to alter expression levels, most of which peaked between 1-3 days; however, others were delayed and peaked by the 7 day time point, with basal gene expression returning by 14 and 28 day timepoints [40]. Our findings suggest that the timing of these genomic changes closely correlate with RAGE protein expression. This observation was further verified by IF staining with anti-RAGE antibody on tissue sections, where the same pattern of expression was observed, thus further validating ^{64}Cu-Rho-G4-CML as an effective RAGE-targeted imaging agent.

Utility and future applications

RAGE's contribution and central involvement in numerous disease processes, which makes it ideal for both targeted therapy and imaging beyond the cardiovascular system, grant this probe the potential for numerous applications, such as RAGE imaging in cancer [41]. RAGE has been identified as a key player in cancer progression; thus, several promising RAGE-targeted therapies have been proposed for cancer treatment [42]. ^{64}Cu-Rho-G4-CML would be an optimal RAGE-targeted imaging agent for cancer as it has been suggested that HSA alone exhibits targeting towards tumor tissue, rendering ^{64}Cu-Rho-G4-CML

both actively and passively targeted to RAGE-expressing cancers [43]. Furthermore, CML alone has been implicated in cancer risk, such as in estrogen-negative breast cancer where its presence predicts poor prognosis [44].
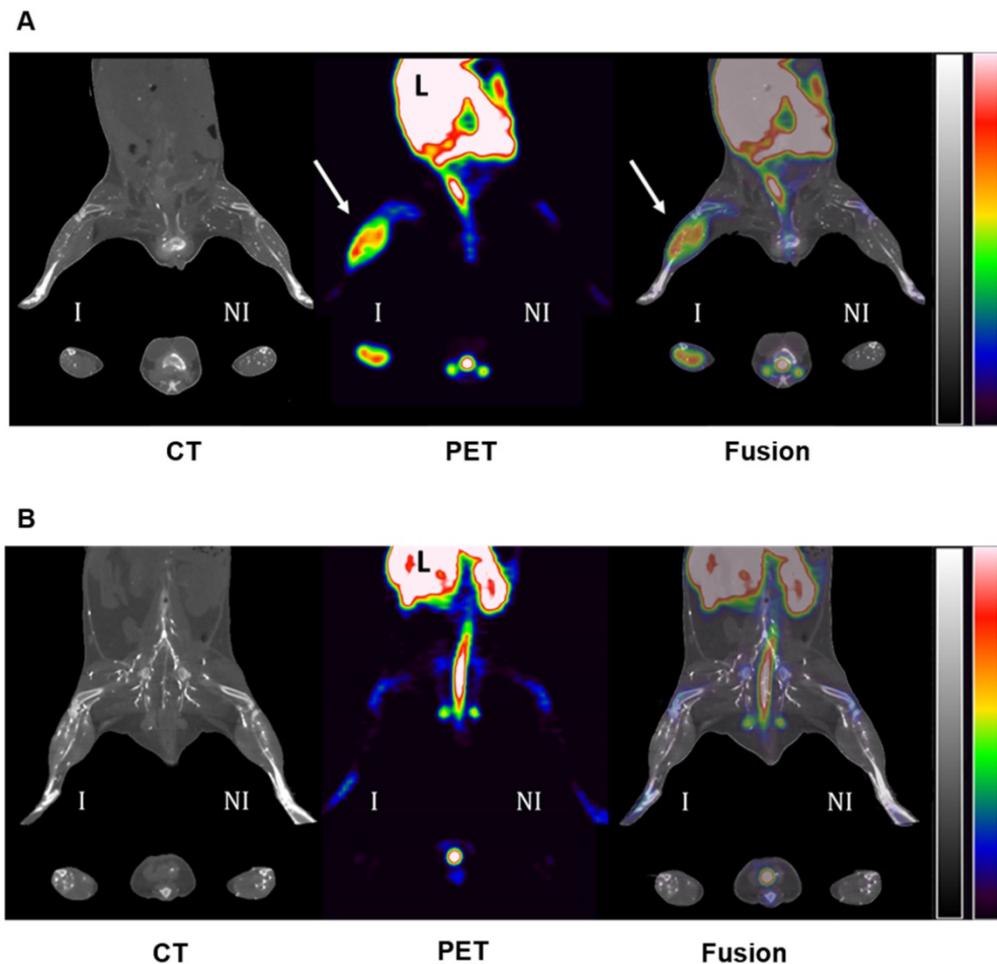
Figure 6. Representative PET-CT images of ⁶⁴Cu-Rho-G4-CML **(A)** and ⁶⁴Cu-Rho-G4-HSA **(B)** in a murine model of hindlimb ischemia. Images were acquired 60 min after intravascular injection of radiotracers and vascular X-ray contrast agent into mice at 1 week following surgical ligation of the right femoral artery. RAGE-targeted ⁶⁴Cu-Rho-G4-CML significantly accumulated within the ischemic hindlimb (yellow arrows) as compared to contralateral non-ischemic hindlimb. Significant uptake was also visible in the liver (L) and feces. There was no noticeable uptake of non-targeted ⁶⁴Cu-Rho-G4-HSA within either ischemic or non-ischemic hindlimbs. CT images are scaled from -1300 to 2100 (HU) and PET images are scaled from 0.5 to 5.0 (%ID/g).
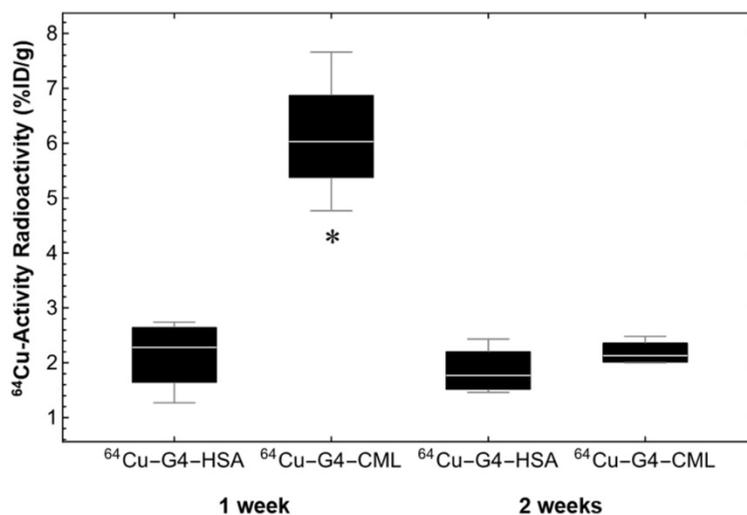
Figure 7. Quantification of PET-CT images acquired at 60 min post injection of ⁶⁴Cu-Rho-G4-CML (RAGE-targeted) or ⁶⁴Cu-Rho-G4-HSA (non-targeted) at 1 and 2 weeks post-surgical ligation of the right femoral artery in C57BL/6 mice. There was a statistically significant increase of ⁶⁴Cu-Rho-G4-CML in ischemic hindlimb at 1 week after ligation as compared with non-targeted ⁶⁴Cu-Rho-G4-HSA. Moreover, there was no significant difference at 2 weeks post ligation. * $P < 0.05$ vs. ⁶⁴Cu-Rho-G4-HSA.
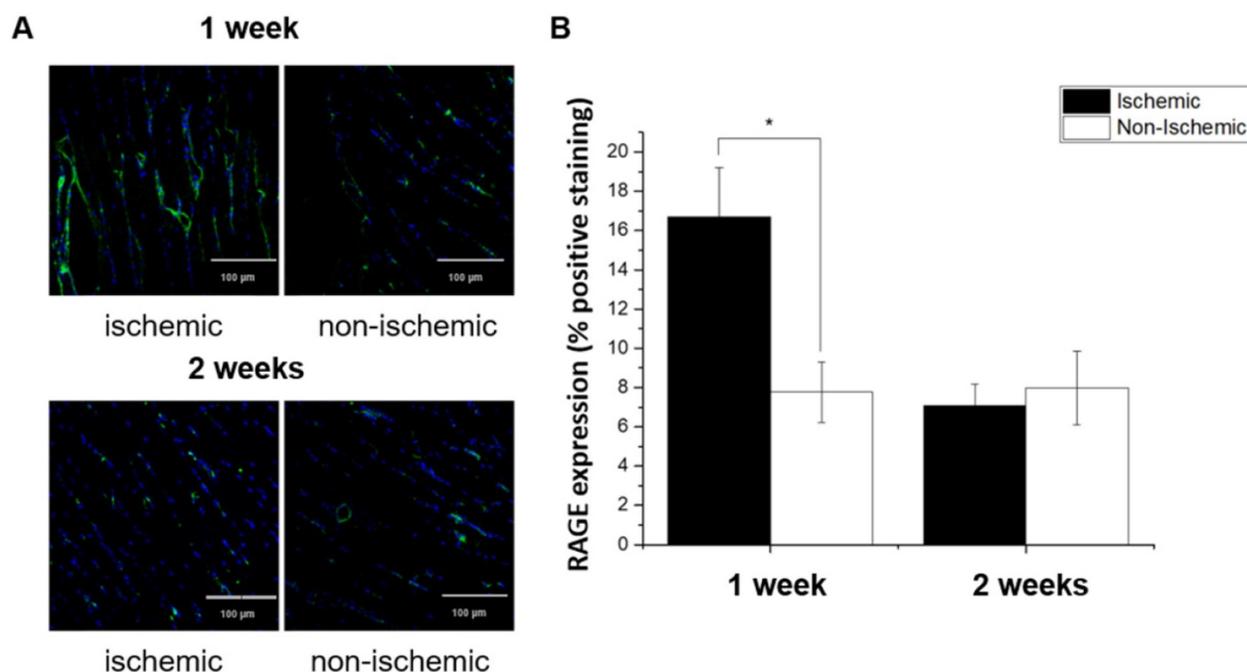
Figure 8. (A) Confocal immunofluorescence images of ischemic and non-ischemic hindlimb muscle sections stained with fluorescein-labeled anti-RAGE antibody (green) and co-stained with nuclear stain (DAPI, blue). **(B)** Quantitative analysis confirmed that ischemic muscle sections at 1 week post ligation demonstrate significant RAGE-positive staining as compared with non-ischemic sections. At 2 weeks post ligation, RAGE-positive staining returned to baseline levels. * $P < 0.05$ vs. non-ischemic hindlimb.

Despite the promise of this probe for RAGE-targeted imaging, it is not without limitations. The size of 64Cu-Rho-G4-CML will not allow it to cross the blood-brain barrier, rendering it ineffective for neurological assessments. Additionally, the use of CML as a targeting ligand provides it passive uptake qualities, which in cancer may be advantageous, but for other applications may confer an unwanted degree of non-specific binding. Non-specificity may arise due to the numerous receptors that may bind the CML ligand, such as members of the scavenger receptor family [45]. Our experiments do not demonstrate significant non-specific uptake; however, it is possible that in conditions where other CML receptors may be highly upregulated (such as imaging with concurrent infections), this probe may have limited utility due to non-specific uptake.

Despite its limitations, this probe demonstrates the utility of a multimodal imaging agent that can serve multi-scale purposes and, considering its payload capabilities, could be used in theranostic applications by serving as a targeted drug delivery vehicle.

Methods

Chemical synthesis

For the synthesis of our multimodal imaging agent, an ethylenediamine-core PAMAM dendrimer of generation 4 (PAMAM, G4), characterized by a 4.5 nm diameter, 14 kDa molecular weight, and 64 valencies, was used. PAMAM was dissolved in 100 mM sodium bicarbonate buffer (pH 9.0) to a final concentration of 10 mg/mL with magnetic stirring. The first stage of the synthesis consisted of blocking thirty-two (50%) dendrimer's free amine groups with sulfosuccinimidyl acetate (Thermo Scientific, USA). Next, 16 free amine groups (25%) were conjugated with bifunctional p-SCN-Bn-NOTA for copper-64 (64Cu) labeling and 8 groups (12.5%) with amine-reactive tetramethylrhodamine succinimidyl ester as a fluorophore. Five to eight (8-12.5%) amine groups of PAMAM dendrimer were linked with RAGE ligand Nε-(carboxymethyl)lysine (CML)-modified HSA for the targeted probe or unmodified (HSA) as a control. These chemicals were crosslinked to the dendrimer's amine groups via succinimidyl-(N-methyl-polyethylene glycol) (Thermo Scientific, USA). The pH was then immediately adjusted to 8.5 with 1 M NaOH and the reaction proceeded for 2 h at room temperature. After each step of the synthesis, the products were purified using ultrafiltration with deionized water using 10k or 100k MWCO Amicon Ultra-15 filters (Millipore, USA). The final nanoparticle construct was lyophilized to obtain a crystalline solid. The degree of substitution of each conjugation was controlled by adjusting the stoichiometry of derivatizing agents to PAMAM. Finally, each reaction product was characterized using nuclear magnetic resonance (1H NMR).

Transmission electron microscopy measurements (TEM)

For TEM, a 2.5 µL portion of 100-fold diluted targeted nanoparticles was placed on a 300-mesh carbon film supported by a copper grid and allowed to stabilize for 2 min. A filter paper was then used to remove liquid for thin liquid film formation and then allowed to air dry while covered. Images were obtained using a Jeol 2010 cryo-electron microscope operating at 200 kV, using different degrees of defocus to obtain an adequate bright contrast. Images were recorded on a Gatan UltraScan 2k×2k CCD. These CCD images were processed and analyzed with ImageJ (http://rsbweb.nih.gov/ij/) version 1.48.

Scanning electron microscopy (SEM) and electron dispersion spectroscopy (EDS)

For SEM-EDS, several 3 µL drops of 100-fold diluted targeted nanoparticles were placed on a strip of carbon tape adhered to an SEM sample grid to stabilize for 5 min. A filter paper was used to remove liquid for thin liquid film formation and then, while covered, allowed to air dry. Images were obtained using a Hitachi S4700 scanning electron microscope with Oxford Instruments ISIS EDS X-ray Microanalysis System. SEM images were captured using a 10 kV accelerating voltage, a 10 µA emission current, and a 12 mm working distance, adjusting sample height for coarse focus and low degrees of defocus to obtain adequate secondary electron images and EDS. Images were recorded using a Centaurus BSE detector.

Dynamic light scattering (DLS) and Zeta-potential

Deionized water was filtered using 0.22 µm syringe filters (VWR) to reduce dust artifacts during DLS measurements. Then, Cu-Rho-G4-CML was added at a concentration of 0.1 mg/mL in filtered DI water. 300 µL of the suspension was then analyzed using a Nicomp 380 ZLS particle-sizer. Each measurement had a run time of 2 min, an average intensity of 92 kHz, and channel width of 52k. All measurements were performed at 23 °C. For Z-potential analysis, the sample was prepared in the same manner as DLS, but 300 µL was loaded into an omega-shaped capillary tube and analyzed using a Litesizer 300 (Anton Paar) at 37 °C.

Cytotoxicity

Cytotoxicity of Cu-Rho-G4-CML was assessed similar to previously published studies [46]. HUVECs were seeded in 12-well plates at a density of $1×10^5$. After 24 h, the culture media was replaced and cells were incubated in new media containing varying concentrations of Cu-Rho-G4-CML (from 0.01 to 100 µM) or standard HUVECs media for 24 h. After 24 h, the media was replaced with 0.14% Trypan Blue solution and incubated for 3 min at room temperature. Finally, the percentage of viable cells were analyzed at 20x magnification under a light microscope. 3 fields of view for each well and 3 wells for each concentration were used for analysis.

The stability of ^{64}Cu-Rho-G4-CML in plasma

The stability of multimodal RAGE-targeted dendrimer was measured in plasma for 24 h post radiolabeling with ^{64}Cu. ^{64}Cu-Rho-G4-CML (~5 mCi) was added to 10 mL of plasma kept at 37 °C with stirring. At 0.5, 1, 1.5, 2, 8, 12, and 24 h post radiolabeling, 0.5 mL of plasma sample was collected and centrifuged using 3k MWCO Amicon Ultra-0.5 mL filters (Millipore, USA). The ^{64}Cu radioactivity (counts-per-minute, CPM) and rhodamine fluorescence (at 627 nm) of both filtrate (unbound ^{64}Cu or rhodamine) and recovered liquid (^{64}Cu-Rho-G4-CML) were measured using a gamma well counter (Wizard2, Perkin-Elmer, USA) and fluorescence microplate reader (BioTek, USA), respectively. Stability expressed as the percent of bound ^{64}Cu or rhodamine (% bound) was calculated by dividing radioactivity or fluorescence of recovered liquid by the total radioactivity or fluorescence of the sample. All stability experiments were done in triplicates.

Cell culture

Human umbilical vein endothelial cells (HUVEC) were obtained from the American Type Culture Collection (ATCC, USA) and cultured as a monolayer at 37 °C with 5% CO_2 antibiotic-supplemented minimal essential medium (MEM), 10% fetal bovine serum (FBS), and endothelial cell growth supplement (ECGS) (all purchased from Sigma-Aldrich, USA). Cells were passaged using Accutase (Sigma-Aldrich, USA) and, at passages 4-5, confluent HUVEC cultures were used for experiments.

RNA extraction, reverse transcription PCR and real-time PCR

Total RNA was extracted from HUVECs and incubated in glucose-supplemented medium (5.5-30 mM) for 12 and 24 h using NucleoSpin RNA XS (Machery-Nagel, USA), according to the manufacturer's instructions. RNA integrity was assessed using an Epoch Microplate Spectrophotometer (BioTek, USA). RNA (1 µg) was then reverse transcribed into single-strand DNA using the cDNA Reverse Transcription Kit (Sigma-Aldrich, USA), according to the manufacturer's instructions. Real-time PCR using Syber Green I Reaction Mix

(Illumina Eco) was then performed to evaluate the effect of high glucose concentrations on the expression pattern of RAGE mRNA and to find both optimal glucose concentration and incubation time that results in maximum RAGE expression in HUVECs. Data were analyzed using the 2-$\Delta\Delta$-Ct formula. β-actin was used as a reference gene. The sequences of RAGE primers were: 5′-TGGAACC GTAACCCTGACCT-3′ and 5′-CGATGATGCTGATG CTGACA-3′. Primers used for β-actin were: 5′-TGTG CCCATCTACGAGGGGTATGC-3′ and 5′-GGTACAT GGTGGTGCCGCCAGACA-3′. Amplification and real-time fluorescence detection were performed using the following protocol: an initial denaturation and polymerase activation step for 2 min at 95 °C, followed by 40 cycles of denaturation at 95 °C for 5 s, annealing at 62 °C for 20 s, and extension at 72 °C for 15 s. The mRNA expression levels of RAGE were normalized to β-actin.

Amplification efficiency values for a specific reaction were established using a standard curve of six logarithmic serial dilutions during the assay design, and to verify that this efficiency measurement was reproducible, multiple standard curves were performed. Serial dilutions were assayed for the target and reference gene and the results plotted with the log input concentration for each dilution on the x-axis, and the difference in Ct (target-reference) for each dilution on the y-axis. Measurement of the fluorescence of the SybrGreen dye with non-specific reaction products was controlled for by melting curve analysis for each amplicon.

Cellular binding

HUVEC cells grown on 96-well plates (Costar, USA) at a density of 5×10^5 cells/well were incubated in medium supplemented with 5.5 mM (control) and 14 mM glucose for 12 h to induce the overexpression of RAGE. For fluorescence binding studies, culture medium was replaced with staining buffer containing 10% FBS in pH 7.4 PBS. For binding of radiolabeled probes, cells were first lifted using Accutase and then suspended in 0.6 mL microcentrifuge tubes with staining buffer. A final volume of 100 μL containing a known amount of fluorescent or radiolabeled targeted and non-targeted nanoparticles was then used for binding studies at 37 °C at different times or concentrations. At the end of the indicated incubation period, the supernatant was discarded and unbound material was rapidly removed by washing the plate three times with PBS. The fluorescence intensity was measured with a Hybrid Multimode Microplate Reader (BioTek, USA) with an excitation wavelength of 520 nm and an emission wavelength of 550 nm, and radioactivity was measured using a gamma well

counter Wizard2 (Perkin-Elmer, USA). K_D was calculated by fitting data to the Hill function: $y = V_{max} \times x^n / (k^n + x^n)$

Data from cell-binding studies were fit to the Hill function using OriginPro 2016 (OriginLab, USA) with Levenberg-Marquardt iteration algorithm.

Flow cytometry

HUVEC cells after the treatment with high glucose concentration were lifted using Accutase (Sigma-Aldrich, USA) and centrifuged for 2 min at 300 ×g at 4 °C. The supernatant was discarded, and the cell pellets were resuspended in FACS buffer (10% FBS, 0.01% sodium azide in PBS, pH 7.4). For the competitive binding study, cells were pre-treated with 1:100 dilution of unlabeled anti-RAGE blocking antibody (R&D systems, USA) for 1 h at 37 °C. Cells were subsequently incubated in various concentrations of Rho-G4-CML (125–750 nM) for 1 h at 37 °C, washed twice, resuspended in FACS buffer and analyzed. Percent binding reduction was found by calculating the percent change of the median Rho-G4-CML fluorescence intensity of anti-RAGE-treated cells compared to control cells. For colocalization studies, cells were incubated with FITC-conjugated anti-RAGE monoclonal antibody (Abcam, USA) for 1 h at 4 °C, washed twice with PBS and incubated with nanoparticles for 1 h at 4 °C. Following the incubation, cells were washed twice with PBS and analyzed by FACS ARIA III (Becton-Dickinson, USA). Vertical and horizontal thresholds were determined using fluorescence minus one (FMO) controls.

Immunofluorescence

Immunofluorescence microscopy studies were performed on HUVECs incubated with 5.5 mM or 14 mM glucose for 12 h using both anti-RAGE monoclonal antibody and targeted or non-targeted nanoparticles. Cells were fixed with 4% paraformaldehyde for 10 min at 4 °C and blocked with 1% BSA for 20 min at room temperature. HUVECs were incubated with RAGE-targeted or non-targeted nanoparticles (200 nM, for 1 h at room temperature). Cells were co-stained with DAPI and visualized using an SP8 laser scanning microscope (Leica, Germany) or In Cell Analyzer 2000 (GE Healthcare, USA) at 400× and 200x magnification. Images were analyzed for colocalization using FIJI Coloc2 plugin [47].

Animal model of hindlimb ischemia

All experiments were performed according to the guiding principles of the American Physiologic Society and approved by the Institutional Animal

Care and Use Committee at the University of Illinois at Urbana-Champaign. Hindlimb ischemia was induced in 2−3-month-old male C57BL/6 mice (Jackson Laboratories, USA) using an already established protocol [48]. The mice were anesthetized with 1-3% isoflurane for surgical intervention and imaging. Before the procedure, the skin was prepped with alcoholic iodine solution. An incision was made on the upper thigh of the right leg of each mouse and the femoral artery was ligated with sterile 6-0 non-absorbable silk sutures (Ethicon, USA). Similarly, a mock procedure was performed on the left leg of each mouse where the skin and soft tissue was dissected but the artery remained unaffected. The skin incision was closed with sterile 6-0 nylon sutures (Ethicon, USA) and the animal was placed in the cage for recovery. Surgery resulted in a small postoperative wound and minimal inflammation. Mice underwent RAGE-targeted microPET/CT imaging at 1 and 2 weeks after surgery.

PET-CT imaging

For dynamic PET imaging studies, we used (n = 3) 2−3-month-old male Lewis rats (Charles River, USA). Animals were anesthetized with 1-3% isoflurane and skin prepped using alcoholic iodine solution for surgical jugular vein cut-down procedure. Then, a polyurethane PE-50 catheter was inserted into a jugular vein followed by radiotracer injection and simultaneous 60-min dynamic microPET-CT scanning with a 20% energy window centered at 511 keV, followed by high-resolution anatomic CT using a hybrid microPET-SPECT-CT small animal scanner (Inveon, Siemens Healthcare, USA). Finally, 3D regions of interest (ROIs) were drawn manually around organs to generate blood and tissue activity curves.

At 1 or 2 weeks after surgical induction of hindlimb ischemia, mice were injected intravenously with approximately 3.7 MBq of either the targeted probe ^{64}Cu-Rho-G4-CML (n = 6) or control ^{64}Cu-Rho-G4-HSA (n = 6) for static PET-CT imaging. C57BL/6 mice were anesthetized with isofluorane (1-3%), and a PE-10 polyurethane catheter (Becton Dickinson, USA) was placed into the right jugular vein for radiotracer injection. One hour after radiotracer injection, mice were placed supine on the bed with leg secured and underwent 15-min static PET imaging with a 20% energy window centered at 511 keV, followed by high-resolution anatomic CT using a hybrid microPET-SPECT-CT small animal scanner (Inveon, Siemens Healthcare, USA).

Organ biodistribution

After the terminal imaging session, mice were immediately euthanized, blood samples were collected by cardiac puncture, and tissues were biopsied from select organs for GWC analysis. All samples were weighed, and absolute ^{64}Cu radioactivity measured with a gamma well counter (Perkin-Elmer, USA). Each tissue segment's raw mean counts were corrected for background, decay and weight, and converted to the injected dose percentage per weight (%I.D/g) using a calibration curve with ^{64}Cu aliquots.

Tissue histology

The skeletal muscles from animals at 1 and 2 weeks post ligation were excised, specimens were embedded in TissueTec (Sakura) and snap-frozen in -150 °C methylbutane. Frozen sections (5 µm) were fixed with ice-cold acetone, incubated with FITC-conjugated anti-RAGE monoclonal antibody (1:100, Abcam, USA) for 1 h at room temperature, mounted with DAPI Fluoromount (Southern Biotech, USA), and visualized with a Leica SP8 scanning confocal microscope; images were processed with commercial software (Leica Application Suite X, Leica, Germany). The images were quantified for extent (percentage area) of positive staining in randomly chosen high-powered (200×) fields using algorithms previously validated by our group.

Statistical methods

Paired or unpaired two-tailed Student's t-test was used to determine significance between groups. A P value of less than 0.05 was considered significant (* <0.05, **< 0.005, ***< 0.0005). Data are presented as mean ± standard error (SE). For gamma well counting, the mean and SE were calculated and expressed in %ID/g.

Abbreviations

AGE: advanced glycation end product; CT: computed tomography; HLI: hindlimb ischemia; HUVEC: human umbilical vein endothelial cells; PAMAM: poly(amidoamine) PET: positron emission tomography; RAGE: receptor for advanced glycation end products.

Acknowledgments

France) for providing specific RAGE ligand N-ε-carboxymethyl-lysine-modified human serum albumin used in the experiments, and Dr. Ann-Marie Schmidt for consultations on RAGE biology.

Supplementary Material

Supplementary figures.
http://www.thno.org/v08p5012s1.pdf

Competing Interests

The authors have declared that no competing interest exists.

References

1. Xie J, Mendez JD, Mendez-Valenzuela V, et al. Cellular signalling of the receptor for advanced glycation end products (RAGE). Cell. Signal. 2013; 25: 2185–2197.
2. Malik P, Chaudhry N, Mittal R, et al. Role of receptor for advanced glycation end products in the complication and progression of various types of cancers. Biochim Biophys Acta - Gen Subj. 2015; 1850: 1898–1904.
3. Litwinoff E, Hurtado Del Pozo C, Ramasamy R, et al. Emerging Targets for Therapeutic Development in Diabetes and Its Complications: The RAGE Signaling Pathway. Clin Pharmacol Ther. 2015; 98: 135–44.
4. Schmidt AM, Yan S Du, Yan SF, et al. The biology of the receptor for advanced glycation end products and its ligands. Biochim Biophys Acta - Mol Cell Res. 2000; 1498: 99–111.
5. Yamagishi S, Imaizumi T. Diabetic vascular complications: pathophysiology, biochemical basis and potential therapeutic strategy. Curr Pharm Des. 2005; 11: 2279–99.
6. Barile GR, Pachydaki SI, Tari SR, et al. The RAGE Axis in Early Diabetic Retinopathy. Investig Opthalmology Vis Sci. 2005; 46: 2916.
7. Toth C, Rong LL, Yang C, et al. Receptor for Advanced Glycation End Products (RAGEs) and Experimental Diabetic Neuropathy. Diabetes. 2008; 57: 2337.
8. Singh VP, Bali A, Singh N, et al. Advanced glycation end products and diabetic complications. Korean J Physiol Pharmacol. 2014; 18: 1–14.
9. Hansen LM, Gupta D, Joseph G, et al. The receptor for advanced glycation end products impairs collateral formation in both diabetic and non-diabetic mice. Lab Investig. 2017; 97: 34–42.
10. Salahuddin P, Rabbani G, Khan R. The role of advanced glycation end products in various types of neurodegenerative disease: a therapeutic approach. Cell Mol Biol Lett. 2014; 19: 407–437.
11. Pinkas A, Aschner M. Advanced Glycation End-Products and Their Receptors: Related Pathologies, Recent Therapeutic Strategies, and a Potential Model for Future Neurodegeneration Studies. Chem Res Toxicol.2016; 29: 707-714.
12. Wang K, Zhou Z, Zhang M, et al. Peroxisome Proliferator-Activated Receptor γ Down-Regulates Receptor for Advanced Glycation End Products and Inhibits Smooth Muscle Cell Proliferation in a Diabetic and Nondiabetic Rat Carotid Artery Injury Model. J Pharmacol Exp Ther. 2006; 317: 37-43.
13. Hauner H. The mode of action of thiazolidinediones. Diabetes Metab Res Rev. 2002; 18: S10–S15.
14. Bierhaus A, Nawroth PP. Multiple levels of regulation determine the role of the receptor for AGE (RAGE) as common soil in inflammation, immune responses and diabetes mellitus and its complications. Diabetologia. 2009; 52: 2251–2263.
15. Wendt TM, Tanji N, Guo J, et al. RAGE Drives the Development of Glomerulosclerosis and Implicates Podocyte Activation in the Pathogenesis of Diabetic Nephropathy. Am J Pathol. 2003; 162: 1123–1137.
16. Moore TCB, Moore JE, Kaji Y, et al. The role of advanced glycation end products in retinal microvascular leukostasis. Invest Ophthalmol Vis Sci. 2003; 44: 4457–64.
17. Goova MT, Li J, Kislinger T, et al. Blockade of Receptor for Advanced Glycation End-Products Restores Effective Wound Healing in Diabetic Mice. Am J Pathol. 2001; 159: 513–525.
18. Bierhaus A, Haslbeck K-M, Humpert PM, et al. Loss of pain perception in diabetes is dependent on a receptor of the immunoglobulin superfamily. J Clin Invest. 2004; 114: 1741–1751.
19. Park L, Raman KG, Lee KJ, et al. Suppression of accelerated diabetic atherosclerosis by the soluble receptor for advanced glycation endproducts. Nat Med. 1998; 4: 1025–1031.
20. Kaida Y, Fukami K, Matsui T, et al. DNA Aptamer Raised Against AGEs Blocks the Progression of Experimental Diabetic Nephropathy. Diabetes. 2013; 62.
21. Tekabe Y, Li Q, Rosario R, et al. Development of Receptor for Advanced Glycation End Products–Directed Imaging of Atherosclerotic Plaque in a Murine Model of Spontaneous Atherosclerosis. Circ Cardiovasc Imaging. 2008; 1: 212-219 .
22. Tekabe Y, Luma J, Einstein AJ, et al. A novel monoclonal antibody for RAGE-directed imaging identifies accelerated atherosclerosis in diabetes. J Nucl Med. 2010; 51: 92–7.
23. Tekabe Y, Kollaros M, Li C, et al. Imaging receptor for advanced glycation end product expression in mouse model of hind limb ischemia. EJNMMI Res. 2013; 3: 37.
24. Johnson LL, Tekabe Y, Kollaros M, et al. Imaging RAGE expression in atherosclerotic plaques in hyperlipidemic pigs. EJNMMI Res. 2014; 4: 26.
25. Wolf S, Haase-Kohn C, Lenk J, et al. Expression, purification and fluorine-18 radiolabeling of recombinant S100A4: a potential probe for molecular imaging of receptor for advanced glycation endproducts *in vivo*? Amino Acids. 2011; 41: 809–820.
26. Cary BP, Brooks AF, Fawaz M V, et al. Synthesis and Evaluation of [(18)F]RAGER: A First Generation Small-Molecule PET Radioligand Targeting the Receptor for Advanced Glycation Endproducts. ACS Chem Neurosci. 2016; 7: 391–398.
27. Brumley CL, Kuhn JA. Radiolabeled monoclonal antibodies. AORN J. 1995; 62: 343–50, 353-5; quiz 356-8, 361–2.
28. Kobayashi H, Sakahara H, Hosono M, et al. Improved clearance of radiolabeled biotinylated monoclonal antibody following the infusion of avidin as a "chase" without decreased accumulation in the target tumor. J Nucl Med. 1994; 35: 1677–84.
29. Hofferberth SC, Grinstaff MW, Colson YL. Nanotechnology applications in thoracic surgery. Eur J Cardiothorac Surg. 2016; : ezw002-.
30. Tong H-I, Kang W, Davy PMC, et al. Monocyte Trafficking, Engraftment, and Delivery of Nanoparticles and an Exogenous Gene into the Acutely Inflamed Brain Tissue - Evaluations on Monocyte-Based Delivery System for the Central Nervous System. PLoS One. 2016; 11: e0154022.
31. Kobayashi H, Longmire MR, Ogawa M, et al. Rational chemical design of the next generation of molecular imaging probes based on physics and biology: mixing modalities, colors and signals. Chem Soc Rev. 2011; 40: 4626–48.
32. Labieniec-Watala M, Watala C. PAMAM Dendrimers: Destined for Success or Doomed to Fail? Plain and Modified PAMAM Dendrimers in the Context of Biomedical Applications. J Pharm Sci [Internet]. 2015; 104: 2–14.
33. De Silva RA, Jain S, Lears KA, et al. Copper-64 radiolabeling and biological evaluation of bifunctional chelators for radiopharmaceutical development. Nucl Med Biol [Internet]. 2012; 39: 1099–1104.
34. Sadekar S, Ghandehari H. Transepithelial transport and toxicity of PAMAM dendrimers: Implications for oral drug delivery. Adv Drug Deliv Rev. 2012; 64: 571–588.
35. Sobrevia L, Cesare P, Yudilevich DL, et al. Diabetes-induced activation of system y+ and nitric oxide synthase in human endothelial cells: association with membrane hyperpolarization. J Physiol. 1995; 489 (Pt 1): 183–92.
36. Korsmeyer R. Critical questions in development of targeted nanoparticle therapeutics. Regen Biomater. 2016; 3: 143–7.
37. Criqui MH, Aboyans V. Epidemiology of Peripheral Artery Disease. Circ Res [Internet]. 2015; 116.
38. Niiyama H, Huang NF, Rollins MD, et al. Murine model of hindlimb ischemia. J Vis Exp. 2009; 23: 1035.
39. Orbay H, Hong H, Zhang Y, et al. PET/SPECT imaging of hindlimb ischemia: focusing on angiogenesis and blood flow. Angiogenesis. 2013; 16: 279–87.
40. Paoni NF, Peale F, Wang F, et al. Time course of skeletal muscle repair and gene expression following acute hind limb ischemia in mice. Physiol Genomics. 2002; 11:263–272.
41. Bongarzone S, Savickas V, Luzi F, et al. Targeting the Receptor for Advanced Glycation Endproducts (RAGE): A Medicinal Chemistry Perspective. J Med Chem. 2017; 60: 7213–7232.
42. Khan H, Siddiqui Z, Khan MY, et al. AGEs, RAGEs and s-RAGE; friend or foe for cancer. Semin Cancer Biol. 2018; 49: 44–55.
43. Danhier F, Feron O, Préat V. To exploit the tumor microenvironment: Passive and active tumor targeting of nanocarriers for anti-cancer drug delivery [Internet]. J. Control. Release. 2010; 148: 135–146.
44. Nass N, Ignatov A, Andreas L, et al. Accumulation of the advanced glycation end product carboxymethyl lysine in breast cancer is positively associated with estrogen receptor expression and unfavorable prognosis in estrogen receptor-negative cases. Histochem Cell Biol. 2017; 147: 625–634.
45. Ott C, Jacobs K, Haucke E, et al. Role of advanced glycation end products in cellular signaling. Redox Biol. 2014; 2: 411–429.
46. He Y, Zhu Q, Chen M, et al. The changing 50% inhibitory concentration (IC50) of cisplatin: a pilot study on the artifacts of the MTT assay and the precise measurement of density-dependent chemoresistance in ovarian cancer. Oncotarget. 2016; 7: 70803–70821.
47. Schindelin J, Arganda-Carreras I, Frise E, et al. Fiji: an open-source platform for biological-image analysis. Nat Methods. 2012; 9: 676–82.
48. Hedhli J, Slania SLL, Płoska A, et al. Evaluation of a dimeric-cRGD peptide for targeted PET-CT imaging of peripheral angiogenesis in diabetic mice. Sci Rep [Internet]. 2018; 8: 5401.